# Spatial and Temporal Stress Changes in the Aftershock Sequence Following the Nov. 12, 2017 Sarpol-e Zahab Earthquake

*Shahrokh Pourbeyranvand[1*], Saeed Soltani Moghadam[2], and Abolfazl Komeazi[2]*

1. Assistant Professor of Seismology, Earthquake Prediction National Center, International Institute of Earthquake Engineering and Seismology (IIEES), Tehran, Iran,
* Corresponding Author; email: beyranvand@iiees.ac.ir
2. Ph.D. Candidate, International Institute of Earthquake Engineering and Seismology (IIEES), Tehran, Iran

**Received:** 18/08/2018
**Accepted:** 29/09/2018

## ABSTRACT

*A devastating earthquake with moment magnitude of 7.3 hit Sarpol-e Zahab in the Zagros on November 12, 2017. An intense aftershock sequence was recorded by the permanent and dense temporary seismic networks, which installed rapidly in the epicentral region. The focal mechanisms of the November 2017 aftershocks were gathered (for about 50 events) and derived (for about 10 events) from P-wave polarities and/or waveform modeling, show predominantly thrust movements. The transpressional stress regime in the region is suggested as the driving force for the earthquakes. The temporal variation of the principal stress directions analyzed by subsequent stress inversion in several time intervals following the Nov. 2017 mainshocks. In addition, the spatial stress variations were studied implementing the stress tensor inversion in different clusters of events. These results suggest that the 2017 mainshock ruptures caused both spatial and temporal stress perturbations that continued in time showing a specific character, which was not observed before in the Zagros region.*

**Keywords:**
Earthquake; Focal Mechanism; Inversion; Sarpol-e Zahab; Spatial; Stress; Temporal

## 1. Introduction

Major earthquakes have been shown to significantly influence the stress field in the close vicinity of the rupture. The causative stress field has been reported to rotate significantly for some earthquakes. For example, the MW 7.3 Landers earthquake 1992 in southern California [1-2], the $M_W$ 7.4 Izmit (Turkey) earthquake in 1999 [3], and also several subduction zone earthquakes, such as the $M_W$ 9.0 Tohoku earthquake offshore Japan in 2011, the $M_W$ 8.8 Maule earthquake in Chile in 2010 [4-5] and $M_W$ 6 earthquake doublet in the western South Iceland [6] can be referred to as some evidence.

The convergence between the Arabian plate in the southwest and the Eurasian plate in northeast resulted in the complete closing of the Neo-Tethys Ocean and formation of the Zagros continental collision zone [7]. The north-northeast relative movement of the Arabian plate with respect to Eurasia increases from 18 mm/yr in the west (at longitude of about 46°) to 25 mm/yr in the east (at longitude of about 56°) [8]. This relative movement is causing systems of thrust and strike-slip faulting in the Zagros region. Also, a part of this convergence is transferred to the Alborz and Kopet Dagh [9]. The collision was initiated at ~35 Ma and continued to the current setting at ~12 Ma [10]. The main Zagros reverse fault

(MZRF), mountain frontal fault (MFF), high Zagros fault (HZF) and the main recent fault (MRF) are the major faults in the area. November 12, 2017 Sarpol-e Zahab earthquake took place in the northwestern part of the Zagros, in a location placed among HZF and MFF.

Generally, it was believed that in the Zagros, numerous earthquakes with low small to moderate magnitude occur and a considerable amount of deformation takes place deseismically. Despite the Zagros, in the Alborz, the other mountain range in northern Iran, less often earthquakes happen but they are expected to have large magnitudes. This understanding had been gained in the result of the knowledge obtained through several experiences and studies, describing the rheology of the material and the geodynamic characteristics of the regions. But the occurrence of the Sarpol-e Zahab earthquake with 7.3 magnitude, convinced the researchers to reconsider the assumptions caused this unpredicted event to manifest the obvious misunderstanding of the geodynamic situation of the region. That is why reassessment of the information and knowledge available for the study area is of high importance nowadays.

In this study, stress field orientations are derived based on stress tensor inversion of the earthquake focal mechanism data prior to and following the November 12, 2017 mainshock. Then, we try to use the spatial and temporal partitioning of the data to analyze the temporal and spatial changes of the local stress field in the epicentral area. The data from IRSC (Iranian Seismological Center) catalog (2006 to present) was used and also 10 focal mechanisms during 2017 and 2018 were calculated using polarity method [11]. At least two prominent spatially concentrated clusters of events are observed in the study area, and the data can be divided into two pre and post mainshock events (Figure 1). Stress inversions are implemented on both partitioned datasets and the results are compared in the successive sections.

It should be noted here that according to the geographic location of the study area with respect to the seismic networks, the accuracy of the location and the depths of the events are not high because the events are placed outside the networks. Thus, a relocation method has been employed to reduce the amount of error in the location and the depth of

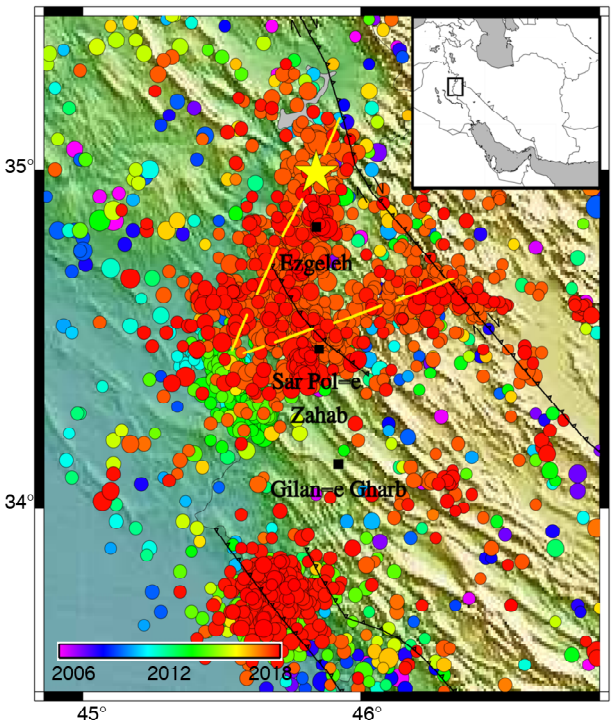


**Figure 1.** Seismicity of the study area, from 2006 to 2018 from IRSC catalog, with color as a scale for the origin time of the events, showing the prominent seismic activity within recent times (red color).

the events. In Figure (1) the seismicity of the area is shown with a color scale based on the origin time of the events. The dataset suffers from the lack of the stations from the neighbor countries which results in high uncertainty in depth estimates and large azimuthal gaps, when calculating the earthquake and source parameters. For this reason, when determining the focal mechanisms by polarity method, the data is limited to the events with gap azimuths less than 180 degrees. However, it is obvious that most of the events are concentrated in two clusters. In the upper clusters, containing the mainshock and demonstrating a V-shape pattern (shown by yellow dash lines in Figure 1) at least two crossing unmapped hidden faults are strongly suggested.

## 2. November 12, 2017 M 7.3 Sarpol-e Zahab Earthquake and its Aftershock Sequence

After the Sarpol-e Zahab main event ($M_W$ 7.3), more than 500 aftershocks (Mn ~2.5) had been recorded by IRSC (Figure 2). The uncertainty in earthquake parameters is unfortunately high due to problems discussed in the previous section. More than 50 well-constrained focal mechanisms were derived from ISC (International Seismological

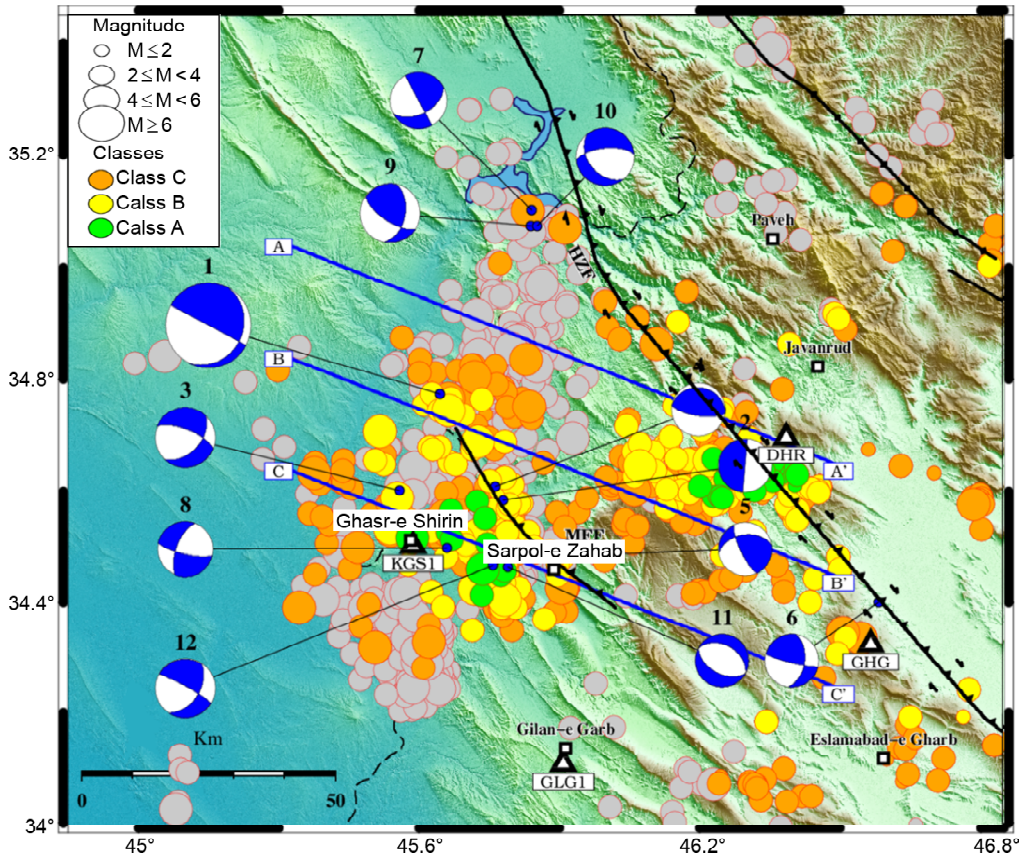


**Figure 2.** Aftershock events, and cross sections.

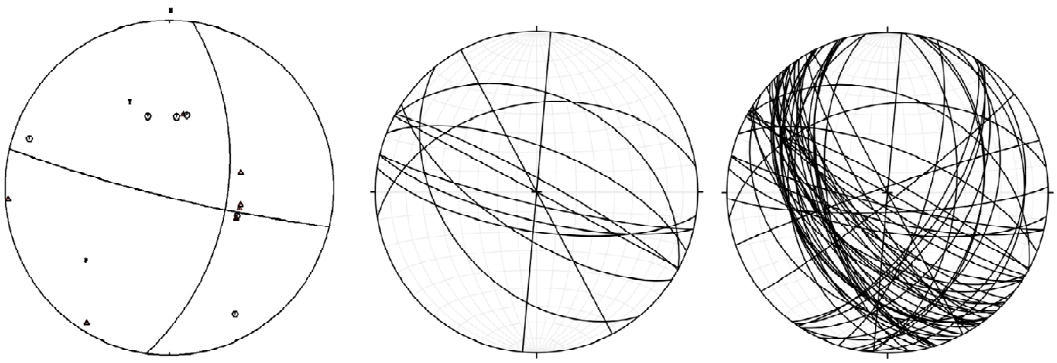

**Figure 3.** (Left): Fault planes of all solutions obtained by using polarity method with four or fewer polarity errors (middle): Lower-hemisphere projections of the focal sphere from Focplt run for one of the events. For polarities, circles represent compressions and triangles represent dilatations. (right): all available fault planes from focal mechanism database.

Centre) for the study area. Furthermore, the computer program, FOCMEC [10] is utilized in this study in order to determine 10 more focal mechanisms for events which had an azimuthal gap less than 180 deg. The algorithm FOCMEC [10], calculates double-couple focal mechanisms based on P-wave polarities and P/SV amplitude ratios. P wave polarities were determined during manual picking of arrival times in SEISAN.

With good station coverage for an earthquake in a region for which the velocity model was well computed, and with well recorded, impulsive P-wave first arrivals, one could get a reliable estimate for the focal mechanism of the event based on whether the first arriving P waves break up or down. When only small number of polarities is available for determination of the solution, they cannot appropriately constrain the nodal plane orientations by themselves. Besides, if the ambiguity of polarities is so severe, the number of possible solutions may be too large [10]. The result of the code for one of the events, all of the focal mechanisms obtained by polarity method and also all of the focal mechanisms available in the study area are shown in Figure (3).

The effects of errors in structure studies can be effectively minimized by using relative earthquake location methods such as the method proposed by Waldhauser and Ellsworth [12]. If the hypocentral separation between two earthquakes is small compared to the event station distance and the scale length of the velocity heterogeneity, then the ray paths between the source region and a common station are similar along almost the entire ray path. In this case, the difference in travel times for two events observed at one station can be attributed to the spatial offset between the events with high accuracy. This is because the absolute errors are of common origin except in the small region where the raypaths differ at the sources. We used double difference method [11] implemented in the HypoDD program to relocate all events recorded from 2010 till the end of June 2018 in the study region. The comparison between the initial (IRSC catalog) and final location results do not show any significant improvement due to large azimuthal gap exists for the majority of events. Nevertheless, the improvements in depth for relocated events cannot be ignored. Three cross-sections perpendicular to the main aftershocks distribution trend (NS-SW) were plotted to investigate the V-shape geometry at depth (Figures 2 and 4).

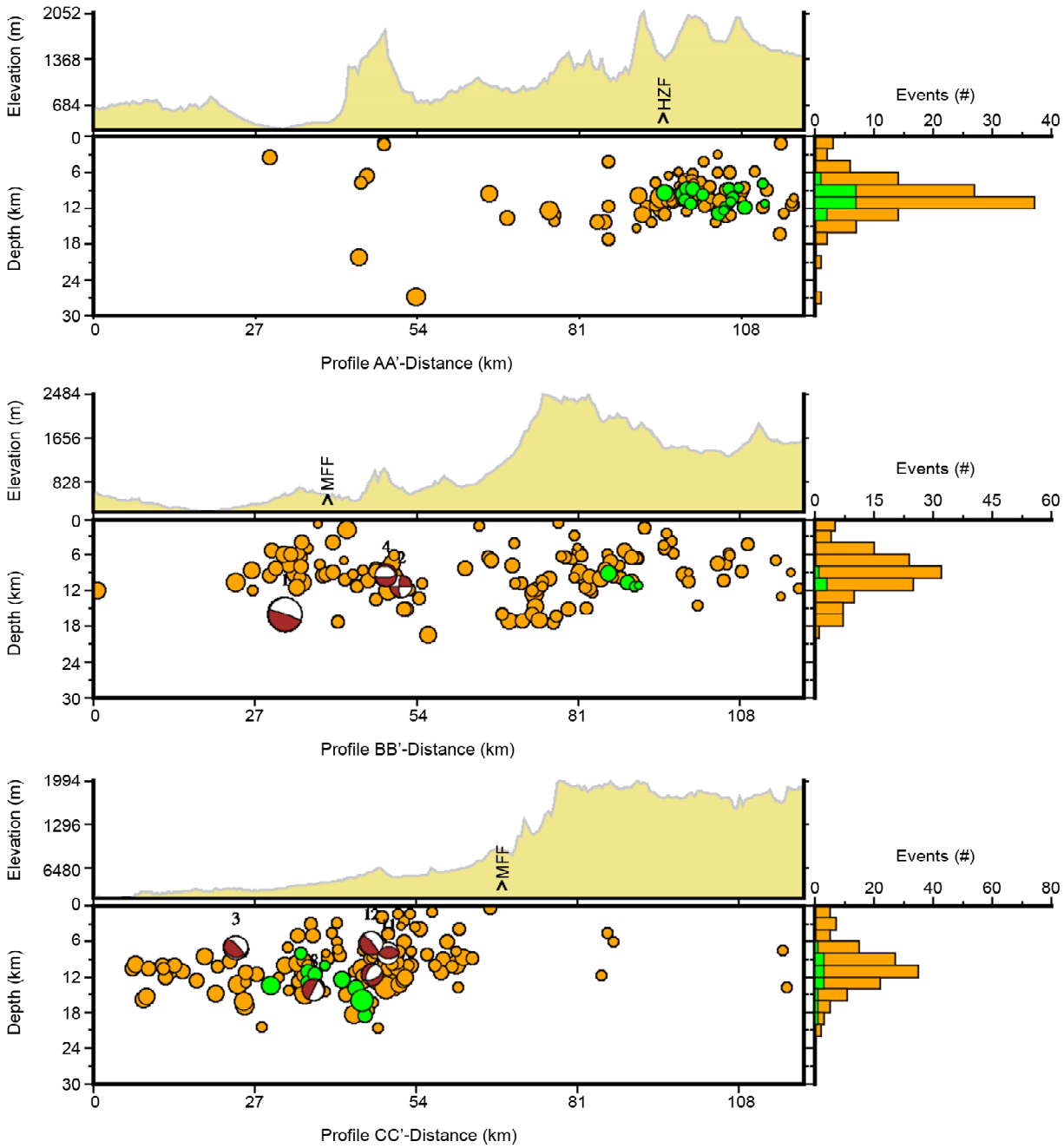


**Figure 4.** Distribution of the aftershock events at depth in the cross sections shown in Figure (2).

Profile AA' shows a dense cluster of events in SE located between 5-16 km in depth. No clear trend can be determined in this profile. In the second profile, BB', two opposite category of event trends are depicted. One in the west side of MFF with a dip toward SE and the other one in the east that is considered to have a dip toward NW. Obvious trends in this profile (shown by a black line) can be a signal of two perpendicular faults. The way well-located events are scattered in the CC' profile, convinced us for depicting a trend line for the third profile which is not very sharp. The relocation of the events thus leads us to consider a hidden fault located in the east side of MFF fault. By the way, more studies with lower uncertainties in focal depths are needed to confirm this probable hidden fault.

By using Kagan's triangle plot [13], we demonstrated the distribution of the event on this diagram, showing their nature of faulting mechanism. From Figure (5), it can be seen that most of the events are reverse. Comparatively fewer but very recent strike-slip events have also taken place in the study area while some rare normal event is evidenced in the current dataset as a result of probable local extensional regimes. In Figure (5) the plunge of *T*, *P* and *B* axis of the earthquake focal mechanisms, are set as RGB parameters, in the way that pure reverse, normal and strike-slip events represent red, blue and green colors respectively. This method can be used to map the variation of faulting mechanisms in the study area as well.

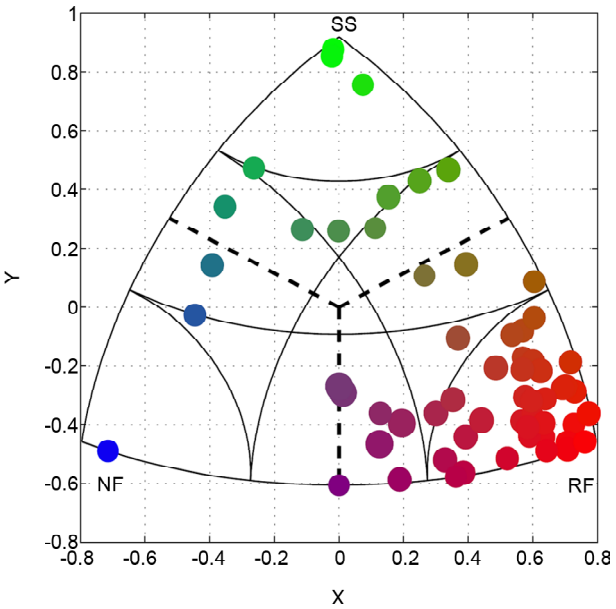


**Figure 5.** Kagan triangle plot of the earthquake focal mechanisms used in this study, showing the nature of faulting mechanisms, with respect to three pure RF (Reverse Faulting), SS (Strike-slip Faulting) and NF (Normal Faulting) regimes by corresponding RGB combinations.

## 3. Spatial and Temporal Distribution of the Focal Mechanisms and Stress Inversions

In order to investigate the spatial and temporal changes in the stress state, we need to classify or subdivide the dataset into groups in space and time. Two main spatially distinct clusters of events can be found in the earthquake focal mechanism data. These clusters are shown as upper and lower ones, $S_1$ and $S_2$ according to their locations, which are placed in northern and southern parts of the study area respectively, indicated with different colors. The limitations in the available data and also seeking the minimum requirements for the inversion procedure, caused the clusters to contain at least about 20 events, with current spatial distribution. The dataset is also temporally subdivided into two periods, before ($T_1$) and after ($T_2$) the mainshock on November 12, 2017 (Appendix I).

The causative stress tensor was calculated by inverting the focal mechanism data using the method of Lund and Slunga [15]. The algorithm is based on a grid search inversion scheme by Gephart and Forsyth [16] with the addition of fault plane selection based on a stability criterion. The method estimates a stress tensor in form of the directions of its three principal stress axes $\sigma_1$, $\sigma_2$ and $\sigma_3$, as well as the relative magnitude of $\sigma_2$, given by $R=(\sigma_1-\sigma_2)/(\sigma_1-\sigma_3)$. Although absolute magnitudes of the stresses cannot be calculated only from focal mechanisms, this approach allows the determination of the direction of the maximum horizontal stress SH [17]. The method further provides confidence limits for the calculated parameters and the preferred nodal planes. The parameter space is searched using 5° steps for the orientations of the stress axes and 0.1 steps for *R* in the grid search. The orientation of SH is calculated as the circular average of all possible SH directions within 95 percent confidence levels. The results of stress inversions are shown in Figures (6) and (7), showing the stress tensor inversion results for available focal mechanisms in the area, which are classified based on their spatial and temporal

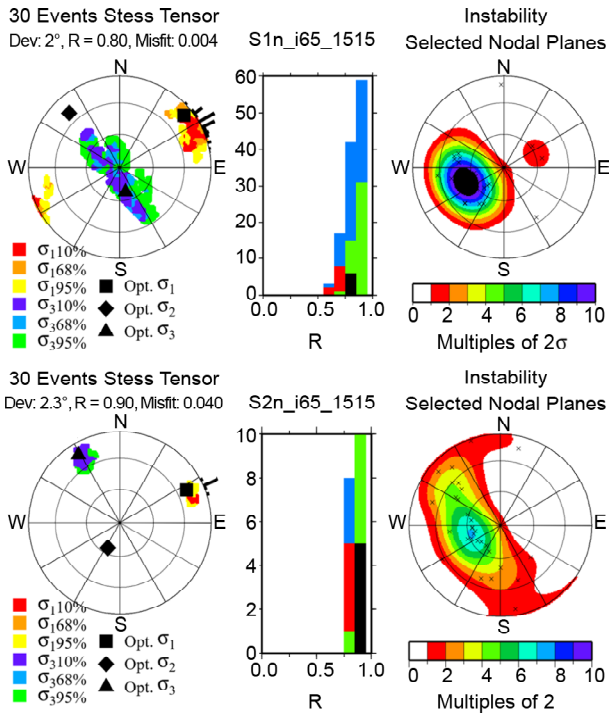


**Figure 6.** Stress inversion results for spatial clusters of the earthquakes.

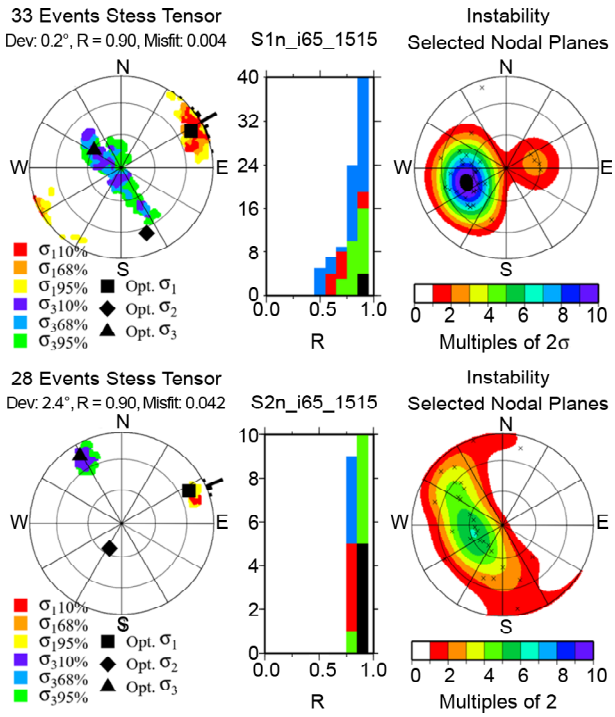


**Figure 7.** Stress inversion results for temporal clusters of the earthquakes.

distributions respectively. In Figure (8) also, both spatial and temporal clustering of the events can be seen in addition to stress inversion results, which will be discussed later.

The orientation of $SH_{max}$ in the $S_1$ is 62.14°, while this orientation for $S_2$ cluster placing south of $S_1$ is 67.28°. This shows a counter-clockwise rotation of $SH_{max}$ of 5.14°, which shows the spatial distribution of stress field in the study area. On the other hand, the pre-mainshock orientation of $SH_{max}$ in the $T_1$ cluster is 59.6°. After the occurrence of the mainshock, the orientation of $SH_{max}$ in the $T_2$ turns to 67.6° and a stable counter-clockwise coseismic rotation of SH of 8°, is observed between these two clusters as well. Variations in the $SH_{max}$ orientations are within the 95 percent confidence level for all subdivisions of the data and the uncertainty in the measurements are also limited to ±6.5° approximately, in all cases that is satisfactory with respect to the accuracy of the more poorly constrained focal mechanisms reaching 15° in most cases.

The stress regime also changes from reverse to strike-slip faulting in response to the earthquakes (Figure 9). The stress regime is determined through the relative size of the stress principal magnitudes that can be estimated in the inversion process [6].

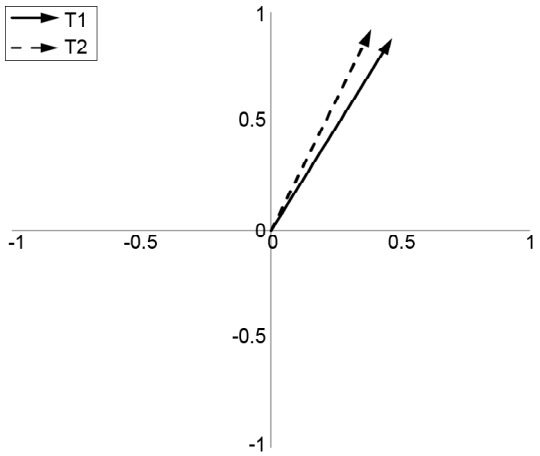


**Figure 8.** The angular difference between $SH_{max}$ directions from two spatial clusters.

In Figure (9), both partitioned datasets can be identified by different colors used. $S_1$ and $S_2$ focal mechanisms are plotted with cyan (0/255/255) and violet (125/0/255) color respectively. The temporal subdivisions of the data are introduced by the color of the *P* axis bars, plotted over the focal mechanisms. For pre mainshock events $T_1$, the *P* axis bars are in teal (0/128/128), while the color for the post mainshock events is magenta (255/0/255).

The resulting $SH_{max}$ direction based on the stress inversion of the focal mechanisms in different clusters and subdivisions of the data, are plotted by

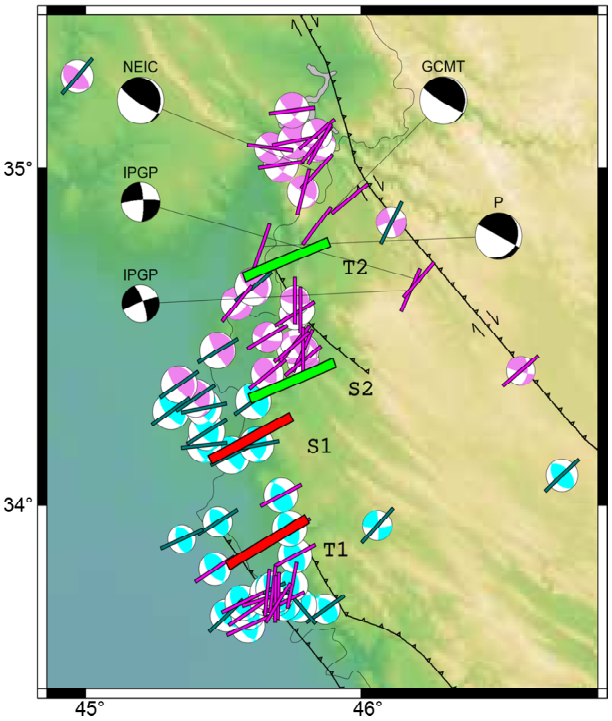


**Figure 9.** spatial and temporal partitioning of the earthquake focal mechanisms and the resulting stress inversion results, shown by different colors corresponding to various stress regimes: red: reverse faulting, green: strike-slip faulting. The focal mechanism data is retrieved from ISC website [14].

red or green bars (8), in the center of gravity of the earthquake focal mechanism clusters, with an annotation describing the name of the subdivision at the right side of the bars ($S_1$, $S_2$, $T_1$ or $T_2$). The color of the bars aims to the stress regime revealed by the inversion procedure with the information obtained about the relative magnitudes of the principal stresses. The stress regime for $T_1$ and $S_1$ are reverse indicated by red color, and the results of the stress inversions for $S_2$ and $T_2$ are plotted in green that refers to strike-slip faulting regime. The focal mechanism of the Sarpol-e Zahab earthquake from NEIC [18] and GCMT [19] can be seen in Figure (9) as well as the solution found through the present study ($P$). Two later earthquake focal mechanisms occurred on 2018-07-22 and 2018-07-25 in the area obtained through IPGP [20] are also plotted in Figure (9).

## 4. Discussion

Many important and interesting facts can be understood by interpretation of the stress tensor inversion results on the amiable focal mechanisms in the area. First of all, the $SH_{max}$ orientations

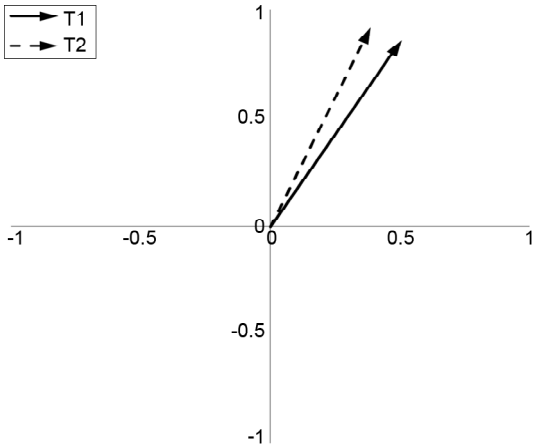


**Figure 10.** The angular difference between $SH_{max}$ directions before and after the main quake (temporal subdivisions of the data).

obtained through this study are very consistent in all cases. It means that the maximum horizontal stress orientation revealed in this study is fully reliable and further structural and tectonic interpretations can trustfully rely on the present results.

The interesting and encouraging achievement of this study is revealing the change in stress field associated with Sarpol-e Zahab earthquake, which is demonstrated both in space and time. The $SH_{max}$ orientation for $S_1$ and $S_2$ groups (spatially partitioned clusters of earthquakes) and also $T_1$ and $T_2$ (temporally partitioned clusters of earthquakes) differ approximately 5° and 8° respectively. The angular difference between the $SH_{max}$ orientations for spatial clusters $S_1$ and $S_2$ is below the uncertainty level of the measurements and may be neglected, but this is not the case for the angular difference between $T_1$ and $T_2$ the temporal subdivisions of the data. Both stress inversion results show a stable counter-clockwise rotation in $SH_{max}$ orientations. The counter-clockwise rotation found between the spatial and temporal subdivisions of the data is illustrated in Figures (8) and (10). The rotation of $SH$ of 8° between its average orientation prior to and after the mainshock is just above the limit of statistical significance for 95 percent uncertainty levels. This difference clearly suggests a counter-clockwise change in stress principal directions after the occurrence of the main event.

Another very important fact revealed by the stress inversion results is the change in stress regime between different subdivisions of the data, i. e. both spatially and temporally partitioned

datasets. The average location of the events for $S_1$ and $S_2$, which are the spatially distinguished datasets, fall comparatively close to each other, in the middle of the study area. The result of the stress inversion for $S_1$ and $S_2$ groups shows reverse and strike-slip stress regimes, which are shown by red and green bars correspondingly. The temporally partitioned datasets include $T_1$ and $T_2$, do not coincide completely with the above-mentioned subdivisions of the data. In fact, the earthquakes happened before the Sarpol-e Zahab earthquake, scatter in both north and south area, but a closer look into the location of the events reminds a relative concentration of the pre mainshock earthquakes in the southern part of the region.

Thus, keeping the overlaps of the $S_1$, $S_2$, $T_1$ and $T_2$ groups in mind, it can be noted that most of the pre mainshock events correspond to the southern cluster of the earthquakes or $S_1$, and most of the post mainshock events or $T_2$ belong to $S_2$ group. For this reason, the result of the stress inversions for these correlated datasets is very similar. The important conclusion that comes out from this comparison is the emphasis on the reliability of the obtained variation in stress state before and after Sarpol-e Zahab earthquake. It should be noted that the similarity of the stress inversion results, in term of the same counter-clockwise rotation of the principal stress orientations for both spatially and temporally partitioned datasets, is reasonable due to the overlap between the datasets.

The last important conclusion by observation of the results of the present study is about the current stress state. As we know now, the stress state in Sarpol-e Zahab area, before the November 12, 2017 *M*7.3 quake was reverse as expected generally in the Zagros as a result of the convergent tectonic environment in the region. But the occurrence of this event has transformed the stress field and has caused the principal stress orientations to rotate about 8° and also has changed the stress regime from reverse to strike-slip. The occurrence of the several earthquakes including two events in July 2018, reported by IPGP with dominant strike-slip mechanism confirmed our finding about the change in stress regime from reverse to strike-slip mechanism. These events may be considered as aftershocks since their location probably falls into the rupture length of the Sarpol-e Zahab mainshock. Further investigations including relocation of the events and determination of earthquake focal mechanisms are needed for obtaining a more comprehensive understanding of the problems in the area.

## 5. Conclusion

50 earthquake focal mechanisms obtained from the local and global agencies and 10 focal mechanisms were determined based on the polarity method to study the stress state in Sarpol-e Zahab area. Relocation of the events could not improve the spatial resolution of the data to clarify an image of any unmapped fault due to the insufficient network coverage. The spatial distribution of the stress filed in the region has been studied by inversion of earthquake focal mechanisms in two geographically distinguished clusters of the events. The $SH_{max}$ has been shown to vary about 5° from 62.14° to 67.28° in specially separated groups of the focal mechanisms. The temporal subdivision of the data revealed that the occurrence of November 12, 2017 *M*7.3 earthquake has caused the principal stress orientations to rotate about 8° from 59.6° to 67.6° and also has changed the stress regime from reverse to strike-slip. The occurrence of many events especially two strike-slip earthquakes in the study area confirmed the finding about the change in stress regime from reverses to strike-slip faulting.

## References

1. Hauksson, E. (1994) State of stress from focal mechanisms before and after the (1992) Landers earthquake sequence. *Bulletin of the Seismological Society of America*, **84**(3), 917-934.

2. Hardebeck, J. and Hauksson, E. (2001) Stress orientations obtained from earthquake focal mechanisms: what are appropriate uncertainty estimates? *Bulletin of the Seismological Society of America*, **91**(2), 250-262.

3. Ickrath, M., Bohnhoff, M., Bulut, F., and Dresen, G. (2013) Stress rotation and recovery in conjunction with the 1999 Izmit MW 7.4 earthquake. *Geophysical Journal International*, **196**, 951-956.

4. Hasegawa, A., Yoshida, K., and Okada, T. (2011) Nearly complete stress drop in the 2011 $M_W$ 9.0 off the Pacific coast of Tohoku Earthquake. *Earth, Planet and Space*, **63**, 703-707.

5. Hardebeck, J. (2012) Coseismic and postseismic stress rotations due to great subduction zone earthquakes. *Geophysical Research Letters*, **39**, L21313, doi: 10.1029/2012GL053438.

6. Hensch, M., Lund, B., Arnadottir, T., and Brandsdottir, B. (2015) Temporal stress changes associated with the 2008 May 29$M_W$ 6 earthquake doublet in the western South Iceland Seismic Zone. *Geophysical Journal International*, **204**(1), 544-554. doi:10.1093/gji/ggv465.

7. Jackson, J. and McKenzie, D. (1984) The active tectonics of the Alpine-Himalayan belt between western Turkey and Pakistan. *Geophys. J. R. Astr. Soc.*, **77**, 185-265.

8. Walpersdorf, A., Hatzfeld, D., Nankali, H., Tavakoli, F., and Nilforoushan, F. (2006) Difference in the GPS deformation pattern of north and central Zagros (Iran). *Geophysical Journal International*, **167**, 1077-1088.

9. Vernant, P., Nilforoushan, F., Hatzfeld, D., Abbassi, M., Vigny, C., Masson, F., Nankali, H., Martinod, J., Ashtiani, A., Bayer, R., Tavakoli, F., and Chéry, J. (2004) Contemporary crustal deformation and plate kinematics in middle east constrained by GPS measurements in Iran and Northern Oman. *Geophysical Journal International*, **157**, 381-398.

10. Madanipour, S., Ehlers, T.A., Yassaghi, A., Rezaeian, M., Enkelmann, E., and Bahroudi, A. (2013) Synchronous deformation on orogenic plateau margins: Insights from the Arabia-Eurasia collision. *Tectonophysics*, **608**, 440-451.

11. Snoke, J.A., Munsey, J.W., Teague, A.C., and Bollinger, G.A. (1984) A program for focal mechanism determination by combined use of polarity and SV-P amplitude ratio data. *Earthquake Notes*, **55**(3), 15.

12. Waldhauser, F. and Ellsworth, W.L. (2000) A double-difference earthquake location algorithm: Method and application to the northern Hayward fault. *Bulletin of the Seismological Society of America*, **90**, 1353-1368.

13. Kagan, Y.Y. (2002) Double-couple earthquake focal mechanism: random rotation and display. *Geophysical Journal International*, **163**, 1065-1072.

14. International Seismological Centre (2016) On-line Bulletin, http://www.isc.ac.uk, Thatcham, United Kingdom.

15. Lund, B. and Slunga, R. (1999) Stress tensor inversion using detailed microearthquake information and stability constraints: Application to Olfus in southwest Iceland. *Journal of Geophysical Research*, **104**(B7), 14947-14964.

16. Gephart, J.W. and Forsyth, D.W. (1984) An improved method for determining the regional stress tensor using earthquake focal mechanism data: application to the San Fernando Earthquake sequence. *Journal of Geophysical Research*, **89**, 9305-9320.

17. Lund, B. and Townend, J. (2007) Calculating horizontal stress orientations with full or partial knowledge of the tectonic stress tensor. *Geophysical Journal International*, **170**, 1328-1335, doi:10.1111/j.1365-246X.2007.03468.x.

18. National Earthquake Information Center (NEIC) U.S. Geological Survey, earthquake.usgs.gov/contactus/golden/neic.php.

19. Global CMT Catalog Search. Global Centroid Moment Tensor Catalog, www.globalcmt.org/CMTsearch.html.

20. Institut De Physique Du Globe De Paris, www.ipgp.fr/en.

# Appendix I

**Table 1.** List of the earthquake focal mechanisms used in this study.

| No. | Date | Time | Longitude | Latitude | Depth | MW | Strike | Dip | Rake | Paz | Ppl | Ref. |
|---|---|---|---|---|---|---|---|---|---|---|---|---|
| 1 | 1/15/1999 | 19:14:14 | 44.97 | 35.27 | 33 | 5.1 | 128 | 29 | 86 | 40.9 | 16 | HRVD |
| 2 | 2/20/2002 | 10:12:29 | 45.648 | 33.738 | 15 | 4.6 | 162 | 58 | 100 | 244.7 | 12.5 | ZUR_RMT |
| 3 | 9/4/2002 | 9:22:10 | 46.063 | 33.944 | 33 | 4.6 | 88 | 80 | 4 | 43.1 | 4.4 | ZUR_RMT |
| 4 | 1/5/2003 | 9:48:47 | 45.478 | 33.952 | 15 | 4.6 | 152 | 54 | 95 | 238.4 | 9 | ZUR_RMT |
| 5 | 1/12/2003 | 14:38:46 | 46.105 | 34.836 | 24 | 4.7 | 251 | 87 | -1 | 206.2 | 2.6 | ZUR_RMT |
| 6 | 2/8/2004 | 20:24:51 | 45.35 | 33.895 | 12 | 4.4 | 164 | 56 | 101 | 246 | 10.3 | ZUR_RMT |
| 7 | 2/12/2004 | 9:20:58 | 45.869 | 33.691 | 12 | 4.6 | 163 | 57 | 114 | 236 | 9.1 | ZUR_RMT |
| 8 | 5/24/2004 | 0:15:00 | 46.728 | 34.086 | 24 | 4.9 | 142 | 42 | 97 | 47 | 3.4 | ZUR_RMT |
| 9 | 11/22/2013 | 18:31:15 | 45.6061 | 34.6459 | 10 | 5.8 | 131.27 | 72.95 | 76.38 | 232.1 | 26.8 | NEIC |
| 10 | 11/22/2013 | 6:51:29 | 45.31 | 34.28 | 18.1 | 5.7 | 139 | 68 | 82 | 235 | 22.6 | GCMT |
| 11 | 11/22/2013 | 6:51:31 | 45.34 | 34.36 | 12.7 | 5.7 | 142 | 72 | 86 | 235.2 | 26.7 | NEIC |
| 12 | 11/22/2013 | 18:30:58 | 45.6105 | 34.3083 | 14 | 5.6 | 146.47 | 68.74 | 90.51 | 236.4 | 23.8 | NEIC |
| 13 | 11/22/2013 | 18:31:04 | 45.4 | 34.32 | 12 | 5.8 | 135 | 70 | 74 | 237.2 | 23.3 | NEIC |
| 14 | 11/22/2013 | 18:31:01 | 45.44 | 34.22 | 13.9 | 5.7 | 134 | 62 | 68 | 239.6 | 14.3 | GCMT |
| 15 | 11/22/2013 | 6:51:25 | 45.4824 | 34.4574 | 6 | 5.6 | 149.48 | 79.63 | 89.26 | 239.8 | 34.7 | NEIC |
| 16 | 11/22/2013 | 18:31:10 | 45.53 | 34.15 | 13.5 | 5.8 | 145 | 65 | 79 | 243.5 | 19.3 | NEIC |
| 17 | 11/24/2013 | 18:05:46 | 45.43 | 34.29 | 15.4 | 5.6 | 25 | 35 | 141 | 259.5 | 18.8 | NEIC |
| 18 | 11/24/2013 | 18:05:42 | 45.6171 | 34.1765 | 14 | 5.4 | 10.32 | 40.7 | 119.46 | 259.8 | 7.6 | NEIC |
| 19 | 11/24/2013 | 18:05:44 | 45.43 | 34.18 | 18.7 | 5.5 | 13 | 41 | 116 | 265 | 6.8 | GCMT |
| 20 | 8/22/2014 | 20:06:05 | 45.7754 | 33.7011 | 10 | 5.1 | 32.58 | 48.28 | 68.11 | 137.9 | 1.1 | NEIC |
| 21 | 8/22/2014 | 20:06:06 | 45.51 | 33.67 | 19.8 | 4.9 | 133 | 57 | 84 | 227.3 | 11.6 | GCMT |
| 22 | 11/3/2017 | 0:20:00 | 45.76 | 34.61 | 9.4 | 4.6 | 98.68 | 70 | 90 | 189 | 25.1 | P |
| 23 | 11/12/2017 | 18:18:25 | 45.84 | 34.83 | 17.9 | 7.4 | 121 | 83 | 82 | 218.4 | 37.5 | GCMT |
| 24 | 11/12/2017 | 18:18:17 | 45.8364 | 34.988 | 21.5 | 7.3 | 122.49 | 79 | 77.78 | 222.5 | 33 | NEIC |
| 25 | 11/12/2017 | 18:18:17 | 45.9592 | 34.9109 | 19 | 7.1 | 32.82 | 18.69 | 177.8 | 232.4 | 41.4 | NEIC |
| 26 | 11/12/2017 | 18:18:19 | 45.794 | 34.93 | 19 |  | 9 | 16 | 153 | 227.4 | 36.2 | IPGP |
| 27 | 11/12/2017 | 18:18:00 | 45.64 | 34.77 | 16 | 7.2 | 118.09 | 90 | 70 | 226.6 | 41.7 | P |
| 28 | 11/12/2017 | 21:33:00 | 45.78 | 34.58 | 11.3 | 4.5 | 5 | 90 | 90 | 95.1 | 45 | P |
| 29 | 11/12/2017 | 22:30:00 | 45.55 | 34.6 | 7.1 | 5.1 | 291.61 | 67.48 | -45.9 | 248.7 | 47.9 | P |
| 30 | 11/13/2017 | 13:12:00 | 45.76 | 34.48 | 11.6 | 4.5 | 260.95 | 43.96 | 22.18 | 214.7 | 19 | P |
| 31 | 12/1/2017 | 20:17:00 | 46.58 | 34.4 | 8 | 4.5 | 103.39 | 83.59 | 39.57 | 229.3 | 21.5 | P |
| 32 | 12/6/2017 | 5:53:00 | 45.84 | 35.1 | 8 | 4.8 | 152 | 90 | 40 | 279.5 | 27 | P |
| 33 | 12/6/2017 | 7:57:00 | 45.66 | 34.5 | 14.1 | 4.7 | 103.23 | 75.52 | -26.57 | 59.4 | 29.1 | P |
| 34 | 12/11/2017 | 14:09:57 | 45.7614 | 35.0786 | 17.6 | 5.4 | 34.91 | 57.62 | 169.7 | 258.6 | 15.9 | NEIC |
| 35 | 12/11/2017 | 14:09:57 | 45.7458 | 35.168 | 19.5 | 5.4 | 36.42 | 61.51 | 164.29 | 262.8 | 9.5 | NEIC |
| 36 | 12/11/2017 | 14:42:42 | 45.67 | 35.06 | 27.9 | 4.8 | 52 | 86 | -179 | 276.9 | 3.8 | GCMT |
| 37 | 12/11/2017 | 14:09:00 | 45.84 | 35.07 | 8 | 5.4 | 123.03 | 67.48 | 45.9 | 243.3 | 11.3 | P |
| 38 | 12/11/2017 | 14:42:00 | 45.85 | 35.07 | 6 | 4.9 | 140.89 | 41.41 | -40.89 | 128.2 | 56.9 | P |
| 39 | 12/20/2017 | 20:01:00 | 45.79 | 34.46 | 8 | 4.5 | 298.5 | 40 | -90 | 27.8 | 85.1 | P |
| 40 | 1/6/2018 | 15:22:09 | 45.7556 | 34.5689 | 11.5 | 5 | 142.68 | 53.86 | 81.65 | 238.8 | 8.6 | NEIC |
| 41 | 1/6/2018 | 15:22:08 | 45.79 | 34.46 | 6 | 5 | 172 | 59 | 119 | 241.5 | 9.5 | IRSC |
| 42 | 1/6/2018 | 15:22:00 | 45.75 | 34.47 | 6.4 | 5 | 298.78 | 83.59 | -39.57 | 248.7 | 31.7 | P |
| 43 | 1/11/2018 | 8:00:40 | 45.7062 | 34.0312 | 17.5 | 5.3 | 172.6 | 38.41 | 119.46 | 62.2 | 9.9 | NEIC |
| 44 | 1/11/2018 | 7:14:16 | 45.7586 | 33.8543 | 13.5 | 5.3 | 153.84 | 40.11 | 92.64 | 62 | 5.1 | NEIC |
| 45 | 1/11/2018 | 6:59:30 | 45.7239 | 33.7131 | 10 | 5.4 | 165.16 | 44.11 | 105.54 | 64.2 | 1.9 | NEIC |
| 46 | 1/11/2018 | 6:59:30 | 45.7397 | 33.9253 | 13.5 | 5.5 | 153.72 | 39.66 | 88.61 | 64.7 | 5.3 | NEIC |
| 47 | 1/11/2018 | 7:55:04 | 45.65 | 33.72 | 12 | 5 | 6 | 55 | 123 | 73.3 | 4.5 | GCMT |
| 48 | 1/11/2018 | 7:14:19 | 45.59 | 33.68 | 16.6 | 5.4 | 137 | 57 | 75 | 238 | 10.8 | GCMT |
| 49 | 1/11/2018 | 8:00:42 | 45.59 | 33.64 | 12.7 | 5.3 | 145 | 50 | 74 | 246.3 | 3.9 | GCMT |
| 50 | 1/11/2018 | 6:59:31 | 45.749 | 33.764 | 19 | 5.5 | 157 | 39 | 72 | 79.7 | 7.4 | IPGP |
| 51 | 1/11/2018 | 7:14:15 | 45.68 | 33.75 | 14 | 5.3 | 152 | 57 | 98 | 236.2 | 11.6 | IRSC |
| 52 | 1/11/2018 | 7:55:00 | 45.70 | 33.73 | 13 | 4.8 | 162 | 54 | 92 | 250.5 | 9 | IRSC |
| 53 | 1/11/2018 | 8:00:39 | 45.69 | 33.72 | 14 | 5.2 | 154 | 47 | 91 | 243.5 | 2 | IRSC |
| 54 | 1/19/2018 | 22:17:59 | 45.47 | 33.81 | 12 | 5 | 138 | 56 | 76 | 238.1 | 9.9 | GCMT |
| 55 | 4/1/2018 | 8:35:26 | 45.79 | 34.43 | 11 | 4.9 | 18 | 70 | -146 | 240 | 37.9 | IRSC |
| 56 | 22/07/2018 | 0:07:26 | 46.179 | 34.645 | 10 | 5.9 | 249 | 83 | -13 | 204.3 | 14.1 | IPGP |
| 57 | 25/08/2018 | 0:13:26 | 46.213 | 34.673 | 13 | 6 | 266 | 82 | -11 | 221.5 | 13.2 | IPGP |